

PCCP

Accepted Manuscript



This is an *Accepted Manuscript*, which has been through the Royal Society of Chemistry peer review process and has been accepted for publication.

Accepted Manuscripts are published online shortly after acceptance, before technical editing, formatting and proof reading. Using this free service, authors can make their results available to the community, in citable form, before we publish the edited article. We will replace this *Accepted Manuscript* with the edited and formatted *Advance Article* as soon as it is available.

You can find more information about *Accepted Manuscripts* in the [Information for Authors](#).

Please note that technical editing may introduce minor changes to the text and/or graphics, which may alter content. The journal's standard [Terms & Conditions](#) and the [Ethical guidelines](#) still apply. In no event shall the Royal Society of Chemistry be held responsible for any errors or omissions in this *Accepted Manuscript* or any consequences arising from the use of any information it contains.

Direct Monitoring of Ultrafast Electron and Hole Dynamics in Perovskite Solar Cells

Piotr Piatkowski,¹ Boiko Cohen,¹ Francisco Javier Ramos,² Maria Di Nunzio,¹ Mohammad Khaja Nazeeruddin,³ Michael Grätzel,³ Shazada Ahmad² and Abderrazzak Douhal^{1*}

¹*Departamento de Química Física, Facultad de Ciencias Ambientales y Bioquímica, and INAMOL, Universidad de Castilla-La Mancha, Avenida Carlos III, S/N, 45071 Toledo, Spain.*

²*Abengoa Research, C/ Energía Solar nº 1, Campus Palmas Altas-41014, Sevilla, Spain.*

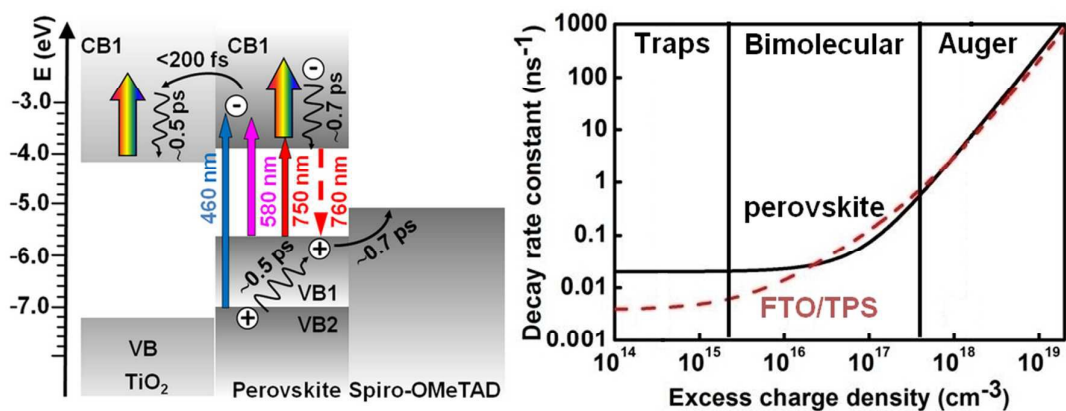
³*Laboratory of Photonics and Interfaces, Institute of Chemical Science and Engineering Faculty of Basic Science, Ecole Polytechnique Federale de Lausanne, CH-1015 Lausanne Switzerland.*

* corresponding author: Abderrazzak Douhal, email: abderrazzak.douhal@uclm.es. Phone: +34-925-265717.

Keywords:

Perovskite, organic-inorganic hybrid solar cells, Spiro-OMeTAD solid hole transporting material, interfacial hole migration, electron injection.

TOC figure and text



Electrons and holes dynamics, internal and surface trap states in perovskite-based solar cells are explored with fs transient absorption spectroscopy.

Abstract

Organic-inorganic hybrid perovskite solar cells emerged as cost effective efficient light-to-electricity conversion devices. Unravelling the time scale and the mechanisms that govern the charge carrier dynamics is paramount for a clear understanding and further optimization of the perovskite based devices. For the classical FTO/bulk titania blocking layer/mesoporous titania/perovskite/Spiro-OMeTAD (FTO/TPS) cell, further detailed and systematic studies of the ultrafast events related to exciton generation, electron and hole transfer, ultrafast relaxation are still needed. We characterize the initial ultrafast processes attributed to the exciton–perovskite lattice interactions influenced by charge transfer to the electron and hole transporters that precede the exciton diffusion into free charge carrier occurring in the sensitizer. Time-resolved transient absorption studies of the FTO/perovskite and FTO/TPS samples under excitation at different wavelengths and at low fluence ($2\mu\text{J}/\text{cm}^2$) indicate the sub-picosecond electron and hole injection into titania and Spiro-OMeTAD. Furthermore, the power-dependent femtosecond transient absorption measurements support the ultrafast charge transfer and show strong Auger-type multiparticle interactions at early times. We reveal that the decays of the internal trap states are the same for both films, while those at surfaces differ. The contribution of the former in the recombination is small, thus increasing the survival probability of the charges in the excited perovskite.

Introduction

As a concept adopted from dye-sensitized solar cells (DSSCs), the hybrid perovskite and its tin analogue $\text{CH}_3\text{NH}_3\text{SnI}_3$ have revolutionized the approach to low-cost solar cell fabrication.¹⁻¹² In a typical solar cell, perovskite sensitizing layer is deposited into mesoporous TiO_2 electrode and then contacted with an electrolyte or solid state hole transporter.¹⁻⁵ Higher efficiencies were achieved by replacing the electrolyte with a solid-hole transporting material such as 2,2',7,7'-tetrakis(*N,N*-di-*p*-methoxyphenylamine)-9,9'-spirobifluorene (Spiro-OMeTAD) or poly(triarylamine).^{1-3,13} It was also found that the perovskites can act not only as a light absorber but also as a charge conductor and that they benefit from a unique combination of both low charge recombination rates and high charge-carrier mobilities.^{1,14-16} Evidence has been reported of charge accumulation in high density of states of $\text{CH}_3\text{NH}_3\text{PbI}_3$ and in Spiro-OMeTAD.¹⁷⁻¹⁸ Power conversion efficiencies (PCEs) of >15% have been reported and were recently pushed to 18 %.^{1-2,19-21}

Recent studies have demonstrated that the morphology of the perovskite capping layer and the crystal structure of the perovskite films play an important role in the photovoltaic performances. Various synthetic approaches have been used to fabricate perovskite thin films, including one and two-step spin-coating processing, vapor deposition and vapor–solution hybrid deposition.^{1-3,14,22-29} It has been showed that the photoluminescence properties of the perovskites strongly depend on the preparation procedure, which results in different size of the resulted crystallites.^{26-28,30}

The earliest ultrafast time-resolved study has shown that the relaxation of the excited state of the perovskite on TiO_2 and Al_2O_3 scaffold is completed on a 1 ns timescale with an estimated half-lifetime of 50 ps and is reductively quenched by Spiro-OMeTAD.³ For $\text{CH}_3\text{NH}_3\text{PbI}_3$, electron and hole diffusion lengths of 130 and 119 nm,

respectively, were calculated,⁸ while for mixed PbCl_2 -derived $\text{CH}_3\text{NH}_3\text{PbI}_3$, still longer distances (1 μm) were suggested.^{7,31} In a different study, the charge-carrier diffusion length in lead iodide perovskite was suggested to exceed 5 μm .³² Recent report on the perovskite single crystal has shown the 175 μm diffusion length of the excited charge-carrier.³³ Time-resolved studies have suggested that the increase of the polycrystallinity enhances the nonradiative deactivation channels, and have shown that the perovskite dynamics critically depends on the specific morphology of the sample.^{26-28,33} For the former, a 0.4 ns time constant was assigned to the electron extraction time when interacting with [6,6]-phenyl-C₆₁-butyric acid methyl ester (PCBM), and 0.66 ns was assigned for the hole transport to Spiro-OMeTAD, with indications of hole transition in the perovskite between two valence bands in 0.4 ps.⁸ A subsequent report has shown that the primary charge separation occurs simultaneously at both junctions with TiO_2 and Spiro-OMeTAD, with ultrafast electron and hole injection taking place within similar timescales, while the charge recombination was significantly slower for TiO_2 compared to Al_2O_3 films.³⁴ Following the generation of the electron-hole pairs, they dissociate within a few picosecond, forming highly mobile charges both in neat perovskite and in perovskite on Al_2O_3 film, resulting in balanced electron and hole mobilities (up to a microsecond timescale).³⁵ Microwave photoconductivity measurements showed that the decay of the mobile charges is slow in $\text{CH}_3\text{NH}_3\text{PbI}_3$ (microsecond time scale).³⁵ Power dependence studies on several perovskites ($\text{CH}_3\text{NH}_3\text{PbI}_3$ (1:1), $\text{CH}_3\text{NH}_3\text{PbI}_3$ (3:1) and $\text{CH}_3\text{NH}_3\text{PbI}_{3-x}\text{Cl}_x$) have suggested that the localisation of electrons and holes is in different regions of the perovskite's unit cell but did not rule out the presence of excitons in the material following photoexcitation.¹⁶ Furthermore, the power dependence indicates that the processes of the charge deactivation are dominated by a two body recombination mechanism.³⁶ It has been

shown that surface passivation results in the retardation of charge recombination between the electrons in the porous titania layers and the holes in the p-type organic conductors.³⁷ Very recently, femtosecond photoluminescence reports on perovskite sensitised on NiO and Al₂O₃ films have proposed a kinetic model that takes into consideration the relaxation of hot holes and electrons and the dynamics of surface-state excitons.³⁸ The charge carrier dynamics in perovskite solar cells were investigated using various time-resolved techniques and two different models have emerged proposed to explain the relaxation of the excited charge carriers.^{8,29,36,38} Following the first model, the optical properties of the perovskites were explained involving three level system, consisting of two valence bands (VB1 and VB2) and a conduction band (CB), while the second one suggests the existence of a charge transfer (CT) state involved in the observed dynamics in the perovskites instead of the VB2 state.²⁹

The spectral features of the generated species, the times of electron and hole diffusion and the excited charge relaxation for perovskites on different electron and hole acceptors were reported. However, additional data for the working cell scheme (involving mesoporous titania, perovskite, and Spiro-OMeTAD) is still needed: (i) the timescale and constants of the early events of electron and hole relaxation within the materials; (ii) electron injection time from perovskite to titania; (iii) whether the electron migration at both material interfaces can compete with the intra-band perovskite electron relaxation and transport; (iv) how the energy excess on the perovskite conduction band (CB) affects such competition relative to the efficiency of the cell; and (v) how the excitation fluence shapes the rate constants and contributions of the electron and hole recombination in the trap states. Here, by using femtosecond (fs) pump-probe visible-near IR transient absorption spectroscopy, we interrogate the ultrafast photo events on FTO/bulk titania blocking layer/mesoporous

titania/perovskite/Spiro-OMeTAD (FTO/TPS) (complete cell) and FTO/bulk titania blocking layer/perovskite (FTO/perovskite, as a reference) films (see SI for the film preparation, and thickness). The experiments unravel the sub-picosecond regime of exciton generation, electron and hole transfer, trapping, migration, relaxation, and fast recombination, in addition to the trap-state dependent of electron-hole recombination. These findings are relevant for a clear understanding of the early events that trigger electron and hole diffusion and transport in perovskite based solar cells and will allow further optimisation.

Results and discussion

Figure 1S shows the steady-state visible absorption spectra of FTO/perovskite films and the FTO/TPS cell. They are similar to those reported in the literature,³ and no significant difference is observed between the two spectra, indicating that they result from similar band-to-band transitions in the perovskite layer. Figure 2S shows the 100-fs and 5-ps gated visible-near IR (NIR) transient absorption spectra (TAS) of both samples after fs-pulse excitation at 460 nm. The value of the pump fluence was 2 $\mu\text{J}/\text{cm}^2$ to avoid multi-exciton interactions (*vide infra*). To examine the effect of FTO on the behavior of the system we measured also the TAS of the system consisting of perovskite layer on glass. Both systems (FTO/perovskite and glass/perovskite) presented identical spectral and dynamical behaviour under the same experimental conditions. Thus in this work we present the results for the FTO/perovskite system. The TAS of the 100-fs delay for both samples are characterized by two bleaching (negative signal) bands at approximately 500 nm and 760 nm and positive bands in the visible (520 – 620 nm) and in the NIR at approximately 850-900 nm (Figure 2S). The bleaching signals are due to depopulation of the VBs, and their dynamics allow characterizing the times for exciton generation, trapping, and hole migration within the

valence bands (Scheme 1). The positive visible and NIR band at 100-fs delay arise due to the absorption of hot electrons and holes. This assignment is based on the comparison between the spectral and kinetic behaviour of both samples at different wavelengths of excitation. The contribution of the hot electron and hole cooling processes in the TA signal was previously reported for perovskite samples interacting with different p- and n-type materials (PCBM, Spiro-OMeTAD, Al₂O₃ and NiO).^{8,38} The positive signals in the visible part of the TA spectra correspond to the dynamics of the excited populations (charge carriers) and thus they give information about the evolution of the formed excitons. At 750 nm excitation, the pulse generates charge carriers predominantly at the top of the valence band (hole) and at the bottom of the conduction band (electron). As a result, the TAS of both samples remain unchanged as the time delay increases from 0.1 to 5 ps (Figure 2Sc). On the other hand, excitation at 460 nm leads to generation of hot electrons and holes followed by a charge cooling to the bottom of the conduction band (electron) and to the top of the valence band (hole). At this excitation wavelength, the TAS (Figure 2S) at 100 fs delay (maximum at ~580 nm) result from the absorption of the hot charge carriers, while those at 5 ps delay (maximum at ~680 nm) are attributed to the charge carriers close to the band gap. The spectra at 5 ps delay at both excitation wavelengths are comparable (bandwidth and position) indicating common relaxation pathway at longer times. Moreover, upon excitation at 460 nm, the sign of the TAS at 5 ps delay the 850-1050 nm region depends on the studied sample: negative for FTO/perovskite, positive for FTO/TPS due to electron, hole and oxidised Spiro-OMeTAD absorption.³⁹ Oxidation of the hole transporter is connected with hole migration from excited perovskite layer to the hole transporter. Thus, the evolution of the TAS in the NIR region provides additional information about the dynamics of the hole transition between the two layers. It should be noted that the absorption spectra of

oxidised Spiro-OMeTAD has a maximum at 500 nm, and thus the TAS for FTO/TPS is affected also by the hole transporter optical properties.³⁹ The comparison of the TAS for FTO/perovskite and FTO/TPS (Figure 2S) shows that the bleaching band of FTO/TPS located at 500 nm has lower intensity than the corresponding band of perovskite, while the bands between 600 and 800 nm for both samples have the same intensity. The absorption of the perovskite in the region between 600 and 800 nm is much higher than the absorption of Spiro-OMeTAD, and the contribution of the hole transporter is thus suppressed.

FTO/perovskite dynamics. To determine the time constants of the above processes, starting with FTO/perovskite (taken as a reference for the FTO/TPS cell study), Figure 1a shows the change over time of the intensity signals gated at selected probe wavelengths. The 560 and 670 nm transients reflect the exciton formation and electron relaxation within CB1 (Scheme 1), respectively. The pump pulse takes the electron from the valence bands to the CB of the perovskite layer (Scheme 1) and, as a result the three-dimensional Wannier-type exciton is formed.⁴⁰ Here we suggest that at the used pump fluence ($2 \mu\text{J}/\text{cm}^2$), the initially formed excitons dissociate within a few picosecond, and thus the observed dynamics on a time scale of a few picosecond results mostly from the exciton behavior, in agreement with previous studies using time-resolved THz spectroscopy.³⁵ The time for the electron cooling derived from the decay (560 nm) and rise (670 nm) of the positive visible bands (520 – 620 nm at 100 fs and 540 – 700 nm at 5 ps) is 0.6 - 0.7 ps. In both transients, a 100 fs rise is seen that precedes the subsequent events. Therefore, we assign it to the exciton formation. Because of the overlap between the positive visible absorption band and the negative signal (500-nm region), the 560 nm transient also shows a fast rise of 250 fs, a value suggesting a combination of an ultrafast (within 100 fs due to exciton formation) and a

slower (0.7 ps due to electron cooling) rising components. Additionally, the 0.6 – 0.7 ps decay (at 560 nm) and rise (at 670 nm) are absent when the samples are excited at 750 nm since at this excitation wavelength the photon energy is not sufficient to create hot electrons and holes (*vide infra*). The signal at 870 nm rises rapidly in 100 fs followed by decay with time constant of 0.5 ps. In similarity with the visible part of the TAS, the shortest component is attributed to the exciton formation. The longer decay time has similar value to the one observed at 560 and 670 nm (0.7 ps), thus it can be attributed to the intraband electron relaxation which, in turn, leads to a radiative e-h recombination in agreement with the shift towards longer wavelengths of the positive TAS band with a maximum at 570 nm (Figure 2S). Note that the radiative e-h recombination can occur on time scales that range from several hundreds of femtoseconds (exciton recombination) to nano- or even milliseconds (as a result of carrier separation and diffusion).^{7-8,35} The 0.7 ps decay at 505 and 0.6 rise at 750 nm of the signals for FTO/perovskite sample reflect the hole migration in the valence bands (Figure 1a and Scheme 1). The kinetic behaviour of the perovskite sample in the region of 500 and 750 nm was previously explained by a two valence band model.^{8,36,38} The 505 and 750 nm bleaches reflect the photobehaviour of the ground state of the sample (depopulation caused by the absorption of the photons). Thus, the observed kinetics are assigned to the photobehaviour of the hole in the VBs. This assignment is further supported by the comparison between decays observed at 480 nm and 505 nm, which show the 0.7 ps rise (VB1 population) and 0.7 ps decay (VB2 depopulation), respectively. Upon excitation at 750 nm, this dynamics is not observed, since the energy of the formed exciton is close to the band gap energy (Scheme 1). We explain this in terms of absence of hole migration between the two valence bands. In a previous femtosecond transient absorption study of PCBM/perovskite/Spiro-OMeTAD sample, several models have

been assessed and the two valence band model has been suggested as the most likely scenario.⁸ Moreover, we observe 100 fs component at 505 and 750 nm, which is attributed to the process of exciton formation. In addition, a careful analysis of the 500-nm region upon excitation at 430 nm shows two overlapping bleaching bands with maxima at 480 and 505 nm (Figure 1b). Their dynamics exhibit a 0.7 ps rising (460 nm) and decaying (505 nm) component, respectively, reflecting hole migration within the VBs. Thus, the 480 nm and 750 nm bands reflect transitions from VB1 to CB1, and the 503 nm band corresponds to a VB2-CB1 transition (Scheme 1). The assignment is based on previous reports and on our results for the samples excited at different excitation wavelengths (460, 580 and 750 nm).^{8,36,38} Upon excitation at 750 nm, the transients in the 500 nm spectral region are the same with the signal at 503 nm being twice as weak as that at 480 nm, which suggests a common origin of these signals (Figure 2S). As the photon energy ($\lambda_{\text{ex}} = 750 \text{ nm}$) is close to the band gap energy we expect to observe only the VB1-CB1 bleaching transition. However, upon excitation at 460 nm, the 505 nm transient shows a 0.6 ps decay, while those at 480 and 750 nm probe are characterized by a 0.7 ps rise characterizing the hole migration processes in VB2 (VB2-CB1 transition) and VB1 (VB1-CB1 transition), respectively. The 0.5 – 0.7 ps hole migration time is comparable to the recently reported value (0.4 ps) upon excitation at 400 nm.⁸ A possible reason of the observed discrepancies might be the difference in the experimental conditions, as well as pump fluctuations. Our results and assignments agree with a recent fs-emission study on perovskite interacting with Al₂O₃ and NiO films, which proposed a three-state model involving hot electron and hole relaxation (fs time-scale) and bulk-state internal conversion from CB1 to VB1 (ns timescale).³⁸ In a recent study, an alternative description of the dual VB of the perovskite electronic structure was proposed. The authors suggested the existence of a dual excited state

composed of a charge transfer state (480 nm) and a charge separated band gap state (760 nm).²⁹ However, it was shown that the differences between these states are observed on a long time scale (hundreds of ps). Following the dual VB model and our data reflecting the exciton dynamics in the initial 5 ps, the model taking into account the movement of the free charge carrier does not describe correctly the studied systems at this timescale.

FTO/TPS dynamics. Next, we examine the photobehaviour of the FTO/TPS cell. The TAS at the near IR region clearly indicate an ultrafast electron injection from the perovskite CB to the titania one (Figure 2Sb). The early peak signal at 870 nm is positive, showing electron absorption on titania and perovskite CBs. The electron injection from perovskite to titania is almost instantaneous and occurs within the first 200 fs, as indicated by the electron absorption rise at 870 nm (Figure 1c,d). For comparison, there is a shorter rising component (100 fs) for the perovskite sample (Figure 1a). Furthermore, this is in agreement with previous time-resolved studies that qualitatively suggested that this process takes place on a fs-timescale.³⁴⁻³⁵ Efficient and ultrafast migration of electrons and holes into TiO₂ and Spiro-OMeTAD is facilitated by the fast and efficient exciton dissociation into mobile charges within the first few picoseconds.^{7,35,40} The 870 nm signal for the FTO/TPS sample subsequently decays in 0.5 ps, similar to the decay and rise of the signals at 560 and 670 nm, respectively, reflecting a fast electron relaxation/cooling within the titania and perovskite CBs (Figure 1c,d). It has been shown that excited titania films with excess energy exhibit a 200-fs decay assigned to free electron trapping.⁴¹ We believe that the difference in times (0.5 ps vs. 0.2 ps) is due to the contribution of a slower electron relaxation (not transferred to titania in this timescale) within perovskite CBs. The time of electron transfer and the difference in the relaxation times within the perovskite and titania CBs are relevant to the efficiency of perovskite-based solar cells. Moreover, the near IR

transients at 860, 900 and 920 nm indicates the contribution of a weak absorption of oxidised Spiro-OMeTAD in this region (Figure 3S).^{3,7} For the FTO/TPS film, the bleaching bands at 750 and 505 nm show ultrafast behaviour: a 100-fs rise and a 0.6-ps decay at 505 nm due to exciton formation and hole migration from VB2 to VB1, respectively, and a 0.75-ps rise at 750 nm due to hole injection into the Spiro-OMeTAD. Upon excitation at 430 nm (Figure 4S), the observed 0.6-ps decaying and rising components at 505 and 460 nm, respectively, confirm the two closely absorbing VBs and the related intraband hole migration (Scheme 1). Note that the resulting oxidised Spiro-OMeTAD has a relatively strong absorption at approximately 500 nm,^{7,16,39} and as a result, the negative intensity of the above bleaching band should be affected by the related positive signal generated on a similar timescale.

Upon pumping at 580 nm, the cell shows similar features, such as 460 nm excitation and evidence of ultrafast electron injection to the titania CB (Figures 1d and 2a). The electron migration (signal at 870 nm) is followed by an intra-band cooling (Figure 2a). The signal is too complex for a simple analysis, as it is a combination of electron thermalisation in titania, relaxation of untransferred electrons, recombination with the hole at the perovskite VB, and absorption of oxidised Spiro-OMeTAD species. The early rise (0.2 ps) at 750 nm combines with the ultrafast bleaching and a 0.5-ps rising component due to radiative exciton recombination. This time constant reflects a fast hole injection from perovskite VB1 to the Spiro-OMeTAD (Scheme 1), which opens the way for recombination of the transferred holes and electrons (for simplicity not shown in Scheme 1).³⁴

Upon pumping at 750 nm, the positive absorption intensity at 870 nm is instantaneous and very weak, later giving a negative signal due to radiative exciton recombination, which indicates that with almost zero excess energy and within the time

scale analyzed here, only a fraction of the electrons at the bottom of the perovskite CB1 are transferred to the titania CB. We believe that in the absence of excess energy at this excitation wavelength, the photogenerated excitons do not dissociate efficiently, in agreement with a recent report showing that thermally activated exciton dissociation and recombination control the carrier dynamic in $\text{CH}_3\text{NH}_2\text{PbI}_3$,³² thus resulting in a lower yield of photon to electricity conversion using NIR photons. The signal at 560 nm now lacks the 0.5-ps decaying component observed upon excitation at 460 and 580 nm (Figure 1c and 2a). At 670 nm, we also observe a 100-fs rise of the signal, and the 0.6-ps decay time is due to electron relaxation within the titania CB. The bleaching signal at 500 nm shows an ultrafast rise without additional ultrafast decaying components, which reflects the exciton creation. Moreover, at this wavelength of excitation, we do not observe the rising and decaying components (~ 0.6 ps) which are present for the FTO/perovskite and FTO/TPS samples in the region of 500 nm bleaching band, upon excitation at 430 and 460 nm. The 750 nm pump pulse creates the hole directly in VB1, and thus the 0.6 ps components resulting from the hole migration are absent. This observation is in agreement with dual VB model. Based on previous reports^{8,36,38} and on this study, Table 1 summarises our suggestion for spectral and dynamical observation at low fluence laser excitation and short time observation.

The relative change in the maximum intensity of the signal pumped at different wavelengths and probed at 870 nm allows comparison of the efficiencies of hot electron injection to titania at different excitation energies of the generated electron. (Figure 2C) The intensity of the positive signal at shorter time delays is mainly due to electron absorption. At longer time delays the signal of the hole transporter builds up. Figure 2c shows the results upon excitation at 460, 580, 650 and 750 nm, taking into account the differences in absorption intensity of the samples at the pump wavelength, its energy

and the pump fluence. Considering the intensity change at the maximum of the signal, it is evident that from the perspective of dynamics within the sub-ps time regime, a higher excitation energy provokes a larger quantum yield of electron injection from perovskite to titania, in agreement with the behaviour of thermally activated excitons.³² The excitation dependent EI efficiency is in agreement with the results presented in a study of the charge transfer mechanism in halide substituted hybrid perovskite solar cell.⁴² For 750 nm pumping, the electron absorption at 870 nm is very weak. Nevertheless, the perovskite layer that is not interacting with titania generates electrons and holes and transports them to produce a photocurrent.^{1,43}

The results for both samples indicate that the dynamics of the processes (electron cooling, hole migration) occurring on a time scale of few picoseconds do not depend on the sample morphology, and result mostly from the behavior of the exciton formed inside the uniform environment of the perovskite lattice. The uniformity of the surroundings of the excitons formed in different parts of the sample arises from the low contribution of the randomly distributed internal trap states.^{16,44} The differences between FTO/perovskite and FTO/TPS samples are mostly due to the small amount of excitons generated on the TiO₂/perovskite interface, which can be trapped in surface trap states or transferred to the oxide directly after excitation. Recent studies suggest that the long diffusion length (~100 nm in the case of polycrystalline CH₃NH₃PbI₃ and ~175 μm for single crystal) of the excited charge carrier is related to enhanced Born effective charges resulting in large static dielectric constant (~70), where the lattice contribution is larger than the electronic one.^{33,44-45} This in turn reduces the carrier scattering and trapping at defects and impurities inside the perovskite.⁴⁴ However, due to the process of charge trapping on the titania oxide/perovskite and perovskite/perovskite crystal interfaces the exciton dissociation into free charge carriers

followed by an efficient diffusion will depend mainly on the sample specific surface morphology.^{26-28,46} This is further supported by a recent report where a crystal-thickness dependent fluorescence lifetime has been found for several perovskite samples and explained in terms of defects at the crystal grain boundaries.⁴⁶

Power dependence studies. It has been suggested that the main phenomenon responsible for the deactivation of the excited states in perovskite layer is the bimolecular e-h recombination.³⁶ The analytical solution of the second-order kinetic equation describing this process gives the linear dependence of the inverse optical density on time. Figure 5S indicates that the ΔOD^{-1} is a linear function of time for lower pump fluences, while the data collected at fluences higher than $30 \mu\text{J}/\text{cm}^2$ deviate from linearity. The observed nonlinearities at higher fluences are caused by the processes of the Auger recombination. Moreover, the obtained results confirm the fact that the monomolecular deactivation does not play important role in the processes of the excited states deactivation. Shortly after fs-excitation, the state saturation is influenced by the carrier-induced Stark effect in both FTO/Perovskite and FTO/TPS films (Figures 3a and 4a). High density of photons absorbed by the sample results in saturation of the excited energy states in the area of the beam spot and it causes the bleaching of the interband optical transitions. Photoexcited carriers are a source of local electric field which leads to a shift of optical transitions and changes in the transition oscillator strengths.⁴⁷⁻⁴⁸ The above described process is recognized as the carrier induced Stark effect and it is characterized by the change in the position and the width of the ground state recovery band. Moreover, strong interactions between the initially created excitons (multiparticle interactions) may generate a new “emitting” transition at a spectral energy that is spectrally shifted with respect to the single exciton “emitting” transition.⁴⁸ This phenomenon is clearly manifested in the change of the position and width of the 760-nm

bleach band of the TAS at short gating times. Alternatively, the short time (0 – 5 ps) behavior of the TAS can be characterized by the dynamic Burstein-Moss band filling model, which takes into account only the TAS broadening at 760 nm.³⁶ This model assumes linear dependence of the band broadening (Burstein-Moss shift of the optical bandgap) on the excited charge density raised to the power of 2/3 (Equation 1S, Supporting Information). However, if one takes into consideration only the state saturation, a continuous change (in terms of change in the FWHM) in the ground state recovery band is to be expected due to absorption saturation even at longer time delays (Figure 3d). Figure 4b shows that the TAS of both systems at 1 ns after the excitation do not differ. This behavior indicates that the power-dependent properties of both FTO/perovskite and FTO/TPS samples at early times can not be considered only in terms of the band filling model (Figure 3d). Thermal diffusion of excitons into mobile carriers, Auger relaxation, radiative recombination and a spatial diffusion of the charge decrease the density of the excited carriers as well as the strength of their interactions, which should prevent the saturation of the conduction band for a relatively long times (1 ns). To better characterize the influence of the dynamical state filling on the optical properties of the FTO/perovskite and FTO/TPS sample, we analyzed their TAS at 0.5 ps and 4 ps in terms of Burstein–Moss model (Figure 5). A good linear dependence of the band broadening on the charge density (Equation 1S) is observed for the data at 4 ps delay, while this dependence at 0.5 ps delay deviates significantly from linearity. This is clear evidence that the early time dynamics are influenced by additional processes and the Burstein-Moss model is only an approximate solution especially at the very early times. Furthermore, the deviation is larger for FTO/TPS than for FTO/perovskite. The observed nonlinearities for FTO/perovskite are due to the processes of the exciton-exciton interaction leading to the Auger relaxation at early times, while for FTO/TPS

additional processes, such as excited charge transfer into the electron and hole transporting materials, influence the resulted curve (Figure 5). As a result of the exciton diffusion occurring within the first few picoseconds, the dynamical behavior of the band gap shift at 4 ps delay results predominantly from the free charge carriers, which in turn do not show the strong Auger interactions, and thus, we observe linear dependence in agreement with the Burstein-Moss model (Equation 1S and Figure 5). Furthermore, in the presence of electron and hole transporters, the conduction band saturation occurs at higher pump fluences even at early times (in less than 2 ps, Figures 3c-d and Equation 1S), which indicates an ultrafast electron transition into titania, in agreement with Burstein-Moss analysis and the above results at lower photoexcitation fluences, and a decrease in the concentration of charge carriers in the conduction band.³⁶

To further examine the importance of the exciton–exciton Auger recombination for the FTO/perovskite and FTO/TPS samples at higher excitation fluences, we have analysed the dependence of the optical density on the pump fluence at 760 nm (2 ps delay) using a nonlinear model (Equations 3S and 4S) that gives the rate constants of the bimolecular (k_{BM}) and Auger (k_A) processes. Good quality fits have been obtained using equation 3S containing only nonlinear terms (Table 2, Figures 3b and 4c). Thus, we conclude that the efficiency of the nonradiative processes connected with trap- and impurity-assisted recombination is low. This result is consistent with theoretical studies on the energy levels of perovskite, which show that the large static dielectric constant reduces carrier scattering and trapping at defects and impurities inside the perovskite, resulting in long diffusion lengths of the excited charge carrier.⁴⁴ However, our results given in Table 2 differ from those previously reported for lead iodide perovskite ($k_A = 3.7 \times 10^{-29} - 1.3 \times 10^{-28} \text{ cm}^6 \text{ s}^{-1}$, $k_{BM} = 9.2 \times 10^{-10} - 9.4 \times 10^{-10} \text{ cm}^3 \text{ s}^{-1}$).¹⁶ In the present study we observe that the major discrepancy is in the values of k_A , which might be due to the

dependence of k_A on the initial density of charge ($\sim n^3$). Note also that the starting values of the carrier densities used in the calculations may lead to a nonlinear dependence of the absorption coefficient on the pump fluence (Equations 5S and 6S and Figure 4d). The value of k_{BM} for the FTO/TPS cell is higher than the corresponding value for FTO/perovskite (Table 2), indicating a higher probability of excited charge recombination in the former. This result suggests the opening of new deactivation pathways in contact with the TiO_2 and Spiro-OMeTAD layers, mainly due to charge migration at their respective interfaces. Additionally, structural order created at the interfaces and the effect of trap states of TiO_2 must be taken into consideration for these recombinations.⁴⁹⁻⁵⁰ Recent spectroscopic studies showed that an important factor, responsible for the performance of the perovskite solar cells, is the interaction between the $\text{CH}_3\text{NH}_3\text{PbI}_3$ and the p- and n-type materials.^{38,45,49-50} Picosecond X-ray absorption spectroscopy has shown that 100 ps after photoexcitation, the electrons are trapped deep in the defect-rich surface shell for anatase titania.⁵¹ Here, the time constants of the internal and surface traps are revealed by flash photolysis experiments that show a bi-exponential decay ($\tau_1 = 0.13 \mu\text{s}$ and $\tau_2 = 2.4 \mu\text{s}$ for FTO/perovskite; $\tau_1 = 0.45 \mu\text{s}$ and $\tau_2 = 2.4 \mu\text{s}$ for FTO/TPS) of the transient absorption band at 580 nm and upon excitation at 460 nm (Figure 6S). These times are attributed to the presence of surface traps (τ_1, k_{Surf}) and internal traps (τ_2, k_{SHR}). For FTO/perovskite, the relative contribution of the k_{SHR} component comprises only 9% of the total signal, while for FTO/TPS, it amounts to 42%. Moreover, the k_{SHR} value ($0.42 \times 10^6 \text{ s}^{-1}$) does not depend on the studied system and is thereby related to the internal energy states of the perovskite. The value of k_{Surf} differs for both samples ($7.7 \times 10^6 \text{ s}^{-1}$ and $2.2 \times 10^6 \text{ s}^{-1}$ for FTO/perovskite and FTO/TPS, respectively, (Table 2). The presence of the TiO_2 mesoporous material may result in a creation of locally ordered TiO_2 /perovskite interfacial region,⁵⁰ and hence can

reduce the number of trap states. The decrease in the total density of the surface traps lowers their contribution to charge deactivation, and the presence of traps derived from the surroundings changes the lifetime of the interfacial nonradiative processes. Figure 6 shows the dependence of the total decay rate constant (R , Equation 4S) for both samples on the excess charge carrier density. The region dominated by Auger recombination (region I) for FTO/perovskite extends over a larger area than the one for FTO/PTS, although the values of both constants are similar. This result is due to the lower probability of k_{BM} in FTO/perovskite, which results in a higher probability of Auger recombination (k_A). The difference in k_{BM} values is also responsible for the discrepancy in region II. However, the differences seen in region III, dominated by nonradiative recombination, are mainly caused by changes in the relative contribution of k_{SHR} and k_{Surf} . To calculate the global rate constant, R , only the k_{SHR} constant was used for FTO/perovskite, while for the FTO/TPS cell R , both k_{Surf} and k_{SHR} components are included.

Conclusion

In summary, we have characterized the photo-induced charge transfer processes within a titania-perovskite-Spiro-OMeTAD cell. We have observed that the electron injection from perovskite to titania is within the first 200 fs, while the electron relaxation times within perovskite and titania CBs are 0.7 ps, and 0.5 ps, respectively. The interfacial hole injection from the perovskite VB to Spiro-OMeTAD occurs in 0.5 ps. The power dependence study of the femtosecond dynamics suggests that significant portion of the generated electrons in the photoexcited perovskite is transferred into titania within first few picoseconds. Furthermore, the nonlinear dependence of the optical band gap on the excited charge density (Burstein-Moss model) for the FTO/perovskite and FTO/TPS systems for early times (< 2 ps) indicate the presence of

the exciton–exciton Auger relaxation and ultrafast charge injection to the electron and hole transporter. We also found that there are two different types of trap states represented by the k_{SHR} and k_{Surf} decay rate constants. The value of k_{SHR} is the same ($0.42 \times 10^6 \text{ s}^{-1}$) for both films, whereas the value of k_{Surf} is $7.7 \times 10^6 \text{ s}^{-1}$ for FTO/perovskite and $2.2 \times 10^6 \text{ s}^{-1}$ for the FTO/TPS cell. The contribution of the trap states to the processes of recombination is small, and thus the survival probability of the charge in perovskite is high. Furthermore, our results show that the presence of the TiO_2 affects the contribution of the surface trap states in the processes of charge recombination. Thus, we expect that optimizing the interface between perovskite and TiO_2 will further improve the overall performance of the system. These data provide new insight into the ultrafast photodynamics within the excited FTO/TPS cell to further optimize the related devices for efficient energy harvesting.

Experimental part

Device Fabrication and Characterization. The current-voltage (J-V) characteristics of a typical TPS solar cell measured under light intensities of 100 mW cm^{-2} (Figure 7S). The reproducibility of these devices made by sequential deposition method was excellent with less than 10% deviation. The short-circuit current density (JSC), open-circuit voltage (VOC) and fill factor (FF), respectively, are 20.46 mA cm^{-2} , 974mV and 0.677, leading to power conversion efficiency of 13.5%. Further details about the device fabrication and characterization are given in the Supporting information.

Femtosecond Transient Absorption Spectrophotometer. The femtosecond (fs) transient UV-visible-near-IR experiments were done using a chirped pulse amplification setup.⁵² It comprises a Ti:sapphire oscillator (TISSA 50, CDP Systems) pumped by a 5

W diode laser (Verdi 5, Coherent). The seed pulse (30 fs, 450 mW at 86 MHz) centred at 800 nm wavelength is directed to an amplifier (Legend-USP, Coherent). The amplified fundamental beam (50 fs, 1 W at 1 kHz) is directed through an optical parametric amplifier for wavelength conversion (CDP Systems). The second (750, 650 and 580 nm) or the fourth (460 nm) harmonic of the output of the OPA was used as the pump. The pump pulse intensity was kept constant at $2 \mu\text{J}/\text{cm}^2$ (460, 580 and 650 nm) or $5 \mu\text{J}/\text{cm}^2$ (750 nm). The instrument response function (IRF) was measured in terms of ΔOD for FTO/titania-spiro-OMeTAD film following an excitation at 460 nm. The signal was fitted by a Gaussian function taking into consideration its derivatives. The obtained value for IRF was ~ 100 fs. The ratio of the spot size of the pump with respect to the probe was always bigger than 3:1. The spot size was measured using the razor (knife)-edge method.⁵³⁻⁵⁴ Further details about the detection system are given in the supporting information.

Flash Photolysis Spectrophotometer. The nanosecond (ns) flash photolysis setup was the same as previously described.⁵⁵ Briefly, it consists of a LKS.60 laser flash photolysis spectrometer (Applied Photophysics) and a Vibrant (HE) 355 II laser (Opotek). To excite the sample, we used the signal from OPO (pumped by a Q-switched Nd:YAG laser, Brilliant, Quantel) at 460 nm. The pump fluence was $80 \mu\text{J}/\text{cm}^2$. To probe the system, we used the light source of a 150 W Xenon arc lamp. The light transmitted through the sample was then dispersed by a monochromator and detected by visible photomultiplier (Applied Photophysics R928), which is coupled to a digital oscilloscope (Agilent Infiniium DS08064A, 600 MHz, 4 GSa/s). The measured IRF of the system was ~ 6 ns. The kinetic traces were collected at 580 nm and were fit by a bi-exponential function.

Acknowledgements

Financial support from MINECO (Spain) through projects PLE2009-0015, MAT2011-25472 (AD), and Torres Quevedo grant (AS). MKN thanks funding from the European Union Seventh Framework Programme [FP7/2007-2013] under grant agreement n° 604032 of the MESO project.

Associated content

Supporting Information

Details of device fabrication, description of transient absorption spectrometer, equations of the recombination dynamic, J-V curve for perovskite cell, steady-state absorption spectra, transient absorption spectra, femtosecond transient absorption decays, flash photolysis decays. This material is available free of charge via the Internet at <http://pubs.rsc.org/>

References

1. M. M. Lee, J. Teuscher, T. Miyasaka, T. N. Murakami, J. J. Snaith, *Science*, 2012, **338**, 643.
2. J. Burschka, N. Pellet, S.-J. Moon, R. Humphry-Baker, P. Gao, M. K. Nazeeruddin, M. Grätzel, *Nature*, 2013, **499**, 316.
3. H.-S. Kim, C. R. Lee, J.-H. Im, K.-B. Lee, T. Moehl, A. Marchioro, S.-J. Moon, R. Humphry-Baker, J.-H. Yum, J.-E. Moser, M. Grätzel, N.-G. Park, *Sci. Re.*, 2012, **2**, 591
4. O. Malinkiewicz, A. Yella, Y. H. Lee, G. M. Espallargas, M. Graetzel, M. K. Nazeeruddin, H. J. Bolink, *Nat. Photonics*, 2014, **8**, 128.
5. D. Liu, T. L. Kelly, *Nat. Photonics* 2014, **8**, 133.
6. S. Kazim, M. K. Nazeeruddin, M. Gratzel, S. Ahmad, *Angew. Chem., Int. Ed.*, 2014, **53**, 2812.
7. S. D. Stranks, G. E. Eperon, G. Grancini, C. Menelaou, M. J. P. Alcocer, T. Leijtens, L. M. Herz, A. Petrozza, H. J. Snaith, *Science*, 2013, **342**, 341.
8. G. Xing, N. Mathews, S. Sun, S. S. Lim, Y. M. Lam, M. Grätzel, S. Mhaisalkar, T. C. Sum, *Science*, 2013, **342**, 344.
9. B. O'Regan, M. Grätzel, *Nature*, 1991, **353**, 737.
10. S. Mathew, A. Yella, P. Gao, R. Humphry-Baker, B. F. E. Curchod, N. Ashari-Astani, I. Tavernelli, U. Rothlisberger, M. K. Nazeeruddin, M. Grätzel, *Nat. Chem.*, 2014, **6**, 242.
11. D. B. Mitzi, S. Wang, C. A. Field, C. A. Chess, A. M. Guloy, *Science*, 1995, **267**, 1473.
12. A. Kojima, K. Teshima, Y. Shirai, T. Miyasaka, *Am. Chem. Soc.*, 2009, **131**, 6050.

13. J. H. Heo, S. H. Im, J. H. Noh, T. N. Mandal, C.-S. Lim, J. A. Chang, Y. H. Lee, H.-J. Kim, A. Sarkar, M. K. Nazeeruddin, M. Grätzel, S. I. Seok, *Nat. Photonics*, 2013, **7**, 486.
14. M. Liu, M. B. Johnston, H. J. Snaith, *Nature*, 2013, **501**, 395.
15. L. Etgar, P. Gao, Z. Xue, Q. Peng, A. K. Chandiran, B. Liu, M. K. Nazeeruddin, M. Grätzel, *J. Am. Chem. Soc.*, 2012, **134**, 17396.
16. C. Wehrenfennig, G. E. Eperon, M. B. Johnston, H. J. Snaith, L. M. Herz, *Adv. Mater.*, 2014, **26**, 1584.
17. H-S. Kim, H.-S.; I. Mora-Sero, V. Gonzalez-Pedro, F. Fabregat-Santiago, E. J. Juarez-Perez, N. -G. Park, J. Bisquert, *Nature Commun.*, 2013, **4**, 2242.
18. P. Qin, A. L. Domanski, A. K. Chandiran, R. Berger, H.-J. Butt, M. I. Dar, T. Moehl, N. Tetreault, P. Gao, S. Ahmad, M. K. Nazeeruddin, M. Grätzel, *Nanoscale*, 2014, **6**, 1508.
19. S. Ryu, J. H. Noh, N. J. Jeon, Y. C. Kim, W. S. Yang, J. Seo, S. I. Seok, *Energy Environ. Sci.*, 2014, **7**, 2614.
20. M. A. Green, A. Ho-Baillie, H. J. Snaith, *Nat. Photonics*, 2014, **8**, 506.
21. W. Nie, H. Tsai, R. Asadpour, J.-C. Blancon, A. J. Neukirch, G. Gupta, J. J. Crochet, M. Chhowalla, S. Tretiak, M. A. Alam, H.-L. Wang, A. D. Mohite, *Science* 2015, **347**, 522.
22. S. Pang, H. Hu, J. Zhang, S. Lv, Y. Yu, F. Wei, T. Qin, H. Xu, Z. Liu, G. Cui, *Chem. Mater.* 2014, **26**, 1485.
23. H. Hu, D. Wang, Y. Zhou, J. Zhang, S. Lv, S. Pang, X. Chen, Z. Liu, N. P. Padture, G. Cui, *RSC Adv.* 2014, **4**, 28964.
24. Q. Chen, H. Zhou, Z. Hong, S. Luo, H. S. Duan, H. Wang, Y. Liu, G. Li, Y. Yang, *J. Am. Chem. Soc.* 2014, **136**, 622.

25. D. Wang, Z. Liu, Z. Zhou, H. Zhu, Y. Zhou, C. Huang, Z. Wang, H. Xu, Y. Jin, B. Fan, S. Pang, G. Cui, *Chem. Mater.* 2014, **26**, 7145.
26. M. De Bastiani, V. D’Innocenzo, S. D. Stranks, H. J. Snaith, A. Petrozza, *APL Mat.*, 2014, **2**, 081509.
27. V. D’Innocenzo, A. R. S. Kandada, M. De Bastiani, M. Gandini, A. Petrozza, *J. Am. Chem. Soc.*, 2014, **136**, 17730.
28. V. Roiati, S. Colella, G. Lerario, L. De Marco, A. Rizzo, A. Listorti, G. Gigli, *Energy Environ. Sci.*, 2014, **7**, 1889.
29. K. G. Stamplecoskie, J. S. Manser, P. V. Kamat, *Energy Environ. Sci.* 2015, **8**, 208.
30. W. Zhang, M. Anaya, G. Lozano, M. E. Calvo, M. B. Johnston, H. Míguez, H. J. Snaith, *Nano Lett.*, 2015, **15**, 1698.
31. E. Edri, S. Kirmayer, S. Mukhopadhyay, K. Gartsman, G. Hodes, D. Cahen, *Nature Commun.*, 2014, **5**, 3461.
32. T. J. Savenije, C. S. Ponseca Jr., L. Kunneman, M. Abdellah, K. Zheng, Y. Tian, Q. Zhu, S. E. Canton, I. G. Scheblykin, T. Pullerits, A. Yartsev, V. Sundström, *J. Phys. Chem.*, 2014, **5**, 2189.
33. Q. Dong, Y. Fang, Y. Shao, P. Mulligan, J. Qiu, L. Cao, J. Huang, *Science*, 2015, **374**, 967.
34. A. Marchioro, J. Teuscher, D. Friedrich, M. Kunst, R. van de Krol, T. Moehl, M. Grätzel, J.-E. Moser, *Nat. Photonics* 2014, **8**, 250.
35. C. S. Ponseca, Jr., T. J. Savenije, M. Abdellah, K. Zheng, A. Yartsev, T. Pascher, T. Harlang, P. Chabera, T. Pullerits, A. Stepanov, J.-P. Wolf, V. Sundström, *J. Am. Chem. Soc.* 2014, **136**, 5189.
36. J. S. Manser, P. V. Kamat, *Nat. Photonics* 2014, **8**, 737.

37. Y. Ogomi, K. Kukihara, S. Qing, T. Toyoda, K. Yoshino, S. Pandey, H. Momose, S. Hayase, *ChemPhysChem*. 2014, **15**, 1062.
38. H.-Y. Hsu, C.-Y. Wang, A. Fathi, J.-W Shiu, C.-C Chung, P.-S Shen, T.-F. Guo, P. Chen, Y.-P. Lee; E. W.-G. Diau, *Angew. Chem. Int. Ed.* 2014, **126**, 9493.
39. U. B. Cappel, E. A. Gibson, A. Hagfeldt, G. Boschloo, *J. Phys. Chem. C* 2009, **113**, 6275.
40. K. Tanaka, T. Takahashi, T. Ban, T. Kondo, K. Uchida, N. Miura, *Sol. State Com.* 2003, **127**, 619.
41. Y. Tamaki, K. Hara, R. Katoh, R.; M. Tachiya, A. Furube, *J. Phys. Chem. C* 2009, **113**, 11741.
42. B.-W. Park, S. M. Jain, X. Zhang, A. Hagfeldt, G. Boschloo, T. Edvinsson, *ACS Nano*, 2015, **9**, 2088.
43. J. M. Ball, M. M. Lee, A. Hey, H. J. Snaith, *Energy Environ. Sci.* 2013, **6**, 1739.
44. M. H. Du, *J. Mater. Chem. A*, 2014, **2**, 9091.
45. Q. Lin, A. Armin, R. C. R. Nagiri, P. L. Burn, P. Meredith, *Nat. Photonics*, 2015, **9**, 106.
46. Y. Li, W. Yan, Y. Li, W. Wang, Z. Bian, L. Xiao, S. Wang, Q. Gong, arXiv:1503.05984v1.
47. A. A. Mikhailovsky, A. V. Malko, A. A. Hollingsworth, M. G. Bawendi, V. I. Klimov, *Appl. Phys. Lett.* 2002, **80**, 2380.
48. V. I. Klimov, in *Semiconductor and Metal Nanocrystals: Synthesis and Electronic and Optical Properties*, ed. V. I. Klimov, Taylor & Francis, New York, 2005, ch. 5, pp. 200 – 2008.
49. R. Lindblad, D. Bi, B.-W. Park, J. Oscarsson, M. Gorgoi, H. Siegbahn, M. Odelius, E. M. J. Johansson, H. Rensmo, *J. Phys. Chem. Lett.* 2014, **5**, 648.

50. V. Roiati, E. Mosconi, A. Listorti, S. Colella, G. Gigli, F. De Angelis, *Nano Lett.* 2014, **14**, 2168.
51. M. H. Rittmann-Frank, C. J. Milne, J. Rittmann, M. Reinhard, T. J. Penfold, M. Chergui, *Angew. Chem. Int. Ed.* 2014, **53**, 5858.
52. M. Ziólek, I. Tacchini, M. T. Martínez, X. Yang, L. Sun, A. Douhal, *Phys. Chem. Chem. Phys.* 2011, **13**, 4032.
53. J. A. Arnaud, W. M. Hubbard, G. D. Mandeville, B. de la Clavière, E. A. Franke, J. M. Franke, *Appl. Opt.* 1971, **10**, 2775.
54. M. A. C. de Araújo, R. Silva, E. de Lima, D. P. Pereira, P. C. de Oliveira, *Appl. Opt.* 2009, **48**, 393.
55. M. Ziólek, C. Martín, L. Sun, A. Douhal, *J. Phys. Chem. C* 2012, **116**, 26227-26238.

Tables and Figure Captions

Scheme 1 A diagram showing the studied transitions along with the time-constants for the related processes in FTO/TPS films at short (< 5 ps) window of observation. For simplicity, the diagram does not show the following processes happening in the devices: excitons dynamics, electrons and holes trapping, recombination, and long-time migration and transport.

Table 1 Time constants and related involved photoinduced events at the gated region within 5 ps window of observation of excited FTO/titania-perovskite-spiro-OMeTAD cell.

Table 2 Charge carriers recombination rate constants from the 760-nm band signal of 460-nm excited FTO/perovskite and FTO/TPS.^a

^aThe Shockley-Read-Hall (k_{SHR}) and k_{Surf} coefficients are obtained from the flash photolysis experiments. K_{BM} and k_{A} are the bimolecular and Auger rate constants. The data were obtained using equation (1), see Supporting information for details.

Figure 1 Representative decays of the femtosecond (fs) transient signals in terms of change in absorbance (ΔOD) at the indicated wavelengths for **(a)** FTO/perovskite. **(b)** Decay of the fs-transient signal of the FTO/perovskite film excited at 430 nm and probed at 460 nm (\circ) and at 505 nm (\bullet). **Inset:** Differential absorption spectra of the FTO/perovskite film excited at 430 nm at selected pump – probe delays. **(c)** as in **(a)** but for FTO/titania-perovskite-spiro-OMeTAD (TPS) films. **(d)** Decay of the fs- transient signal in terms of change in absorbance (ΔOD) of FTO/TPS pumped at 460 nm and probed at 870 nm (\circ) along with the instrument response function (\bullet).

Figure 2 Representative decays of the fs-transient signals of FTO/TPS film in terms of change in absorbance (ΔOD) excited at **(a)** 580 nm and **(b)** 750 nm, and probed at the indicated wavelengths. **(c)** Decay of the fs-transient signal in terms of change in absorbance (ΔOD) of FTO/TPS probed at 870 nm and excited at 460 (Δ), 580 (\blacksquare), 650 (\bullet) and 750 nm (\circ). The signals are corrected taking into account the steady-state absorption intensity and the photon flux at the respective pump wavelength.

Figure 3 (a) Transient absorption spectra normalized to the minimum of intensity at 70 $\mu\text{J}/\text{cm}^2$ pump fluence, and **(b)** kinetics ($\lambda_{\text{obs}} = 760$ nm) of FTO/TPS cell excited at 580 nm at different pump fluences ($\mu\text{J}/\text{cm}^2$): 2, 4, 6, 8, 10, 20, 35, 50, 70. The arrow shows the spectral changes as a function of increasing pump fluence as in **(a)** and **(b)**. Change in the optical density of FTO/perovskite (red squares) and FTO/TPS (black circles) at 760 nm and **(c)** 2 ps and **(d)** 1 ns delay time as a function of pump fluence. The data were fitted by a two level saturable-absorber model (supplementary equation. 5).

Figure 4 Transient absorption spectra of FTO/perovskite film normalized to the minimum of intensity at **(a)** 2 ps and **(b)** 1 ns excited at 580 nm at different pump fluences ($\mu\text{J}/\text{cm}^2$): 2, 4, 6, 8, 10, 20, 35, 50, 70. The arrow shows the spectral changes as a function of increasing power. **(c)** Transient absorption kinetics of FTO/perovskite excited at 580 and probed at 760 nm at different pump fluences ($\mu\text{J}/\text{cm}^2$): 2, 4, 6, 8, 10, 20, 35, 50, 70. The dots represent the experimental data and the solid curves represent the best fits using equation (1), and **(d)** Steady-state absorption value of FTO/perovskite (top) and FTO/TPS (bottom) measured at 580 nm as a function of pump fluence. Fit to the data using Eq. 3 (solid line).

Figure 5. Dependence of the perovskite bandgap shift on the excited carrier densities, according to the Burstein-Moss model. The total optical transition energies for **(a)**

FTO/perovskite and **(b)** FTO/TPS at different fluences ($\mu\text{J}/\text{cm}^2$): 2, 4, 6, 8, 10, 20, 35, 50, 70. The values of the total transition energies were calculated at 0.5 and 4 ps delays ($\lambda_{\text{obs}} = 760 \text{ nm}$, $\lambda_{\text{ex}} = 580 \text{ nm}$). The data at 4 ps were fitted by the linear function while those at 0.5 ps were fitted by polynomial function to show the deviation from Burstein-Moss model (Equation 6S, Supporting Information).

Figure 6 Variation of the total electron-hole recombination decay rate constants of FTO/perovskite (black solid line) and FTO/TPS (red dashed line) with excess charge density. Solid vertical lines show the region dominated by Auger processes (III), radiative recombination (II) and Shockley-Hall-Read recombination in FTO/perovskite sample. The vertical dashed lines and red Arabic numbers indicate the regions where the above processes occur in the FTO/TPS cell.

Scheme 1

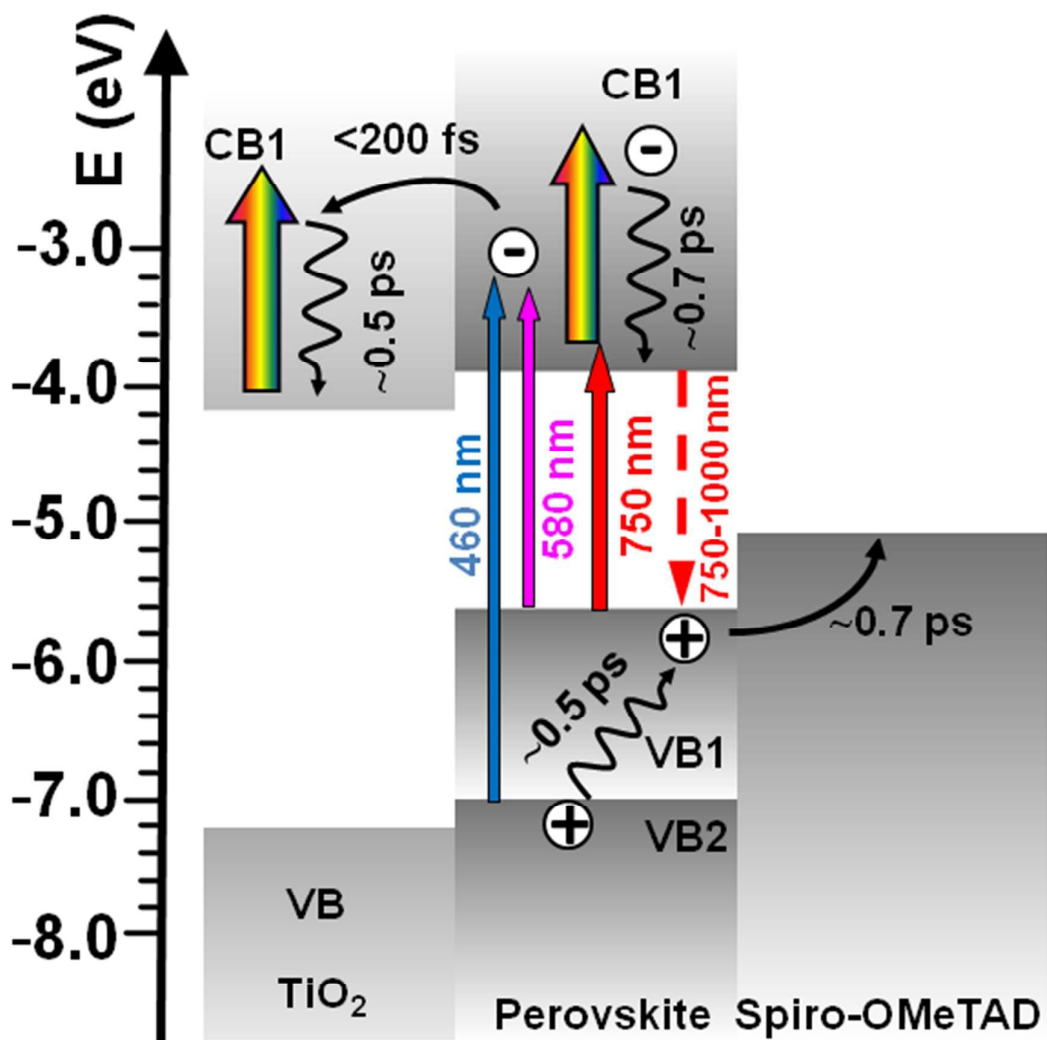


Table 1

Process Spectral Region	Time/ps
Exciton generation 450-520 and 720-770 nm	0.10
Electron injection to titania 520 – 720 and 850 – 1050 nm	0.1-0.2
Electron cooling in perovskite 520 – 720 and 850 – 1050 nm	0.70
Electron thermalisation in titania 520 – 720 and 850 – 1050 nm	0.20 – 0.50
Hole migration VB2-VB1 450 – 520 and 720 – 770 nm	0.50
Hole injection to Spiro-OMeTAD 450 – 770 nm	0.75

Table 2

Sample	k_{SHR} (10^6s^{-1})/(%)	k_{Surf} (10^6s^{-1})/(%)	k_{BM} (10^{10}) $\text{cm}^3 \text{s}^{-1}$	k_{A} (10^{27}) $\text{cm}^6 \text{s}^{-1}$
FTO/perovskite	0.42 (9)	7.7 (91)	2.51	2.82
FTO/TPS	0.42 (42)	2.2 (58)	10	2.01

Figure 1

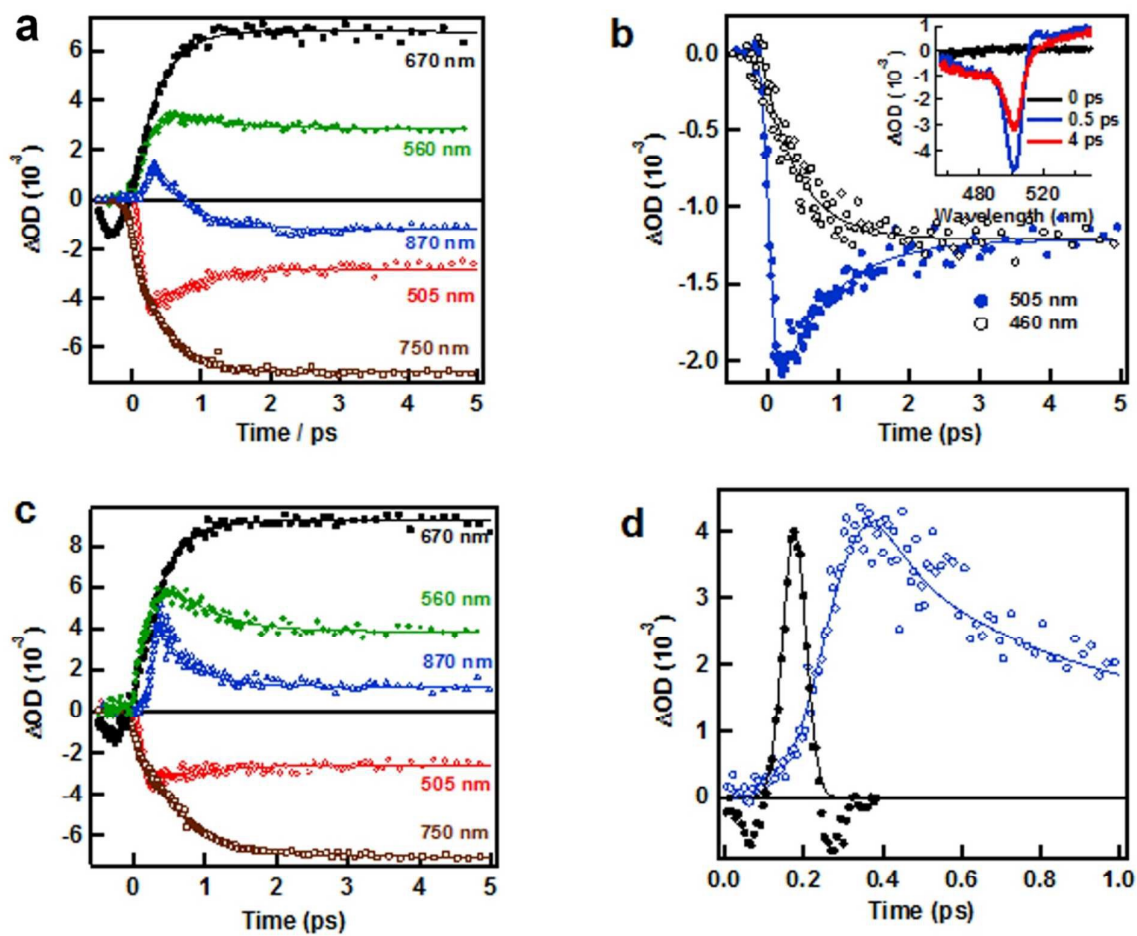


Figure 2

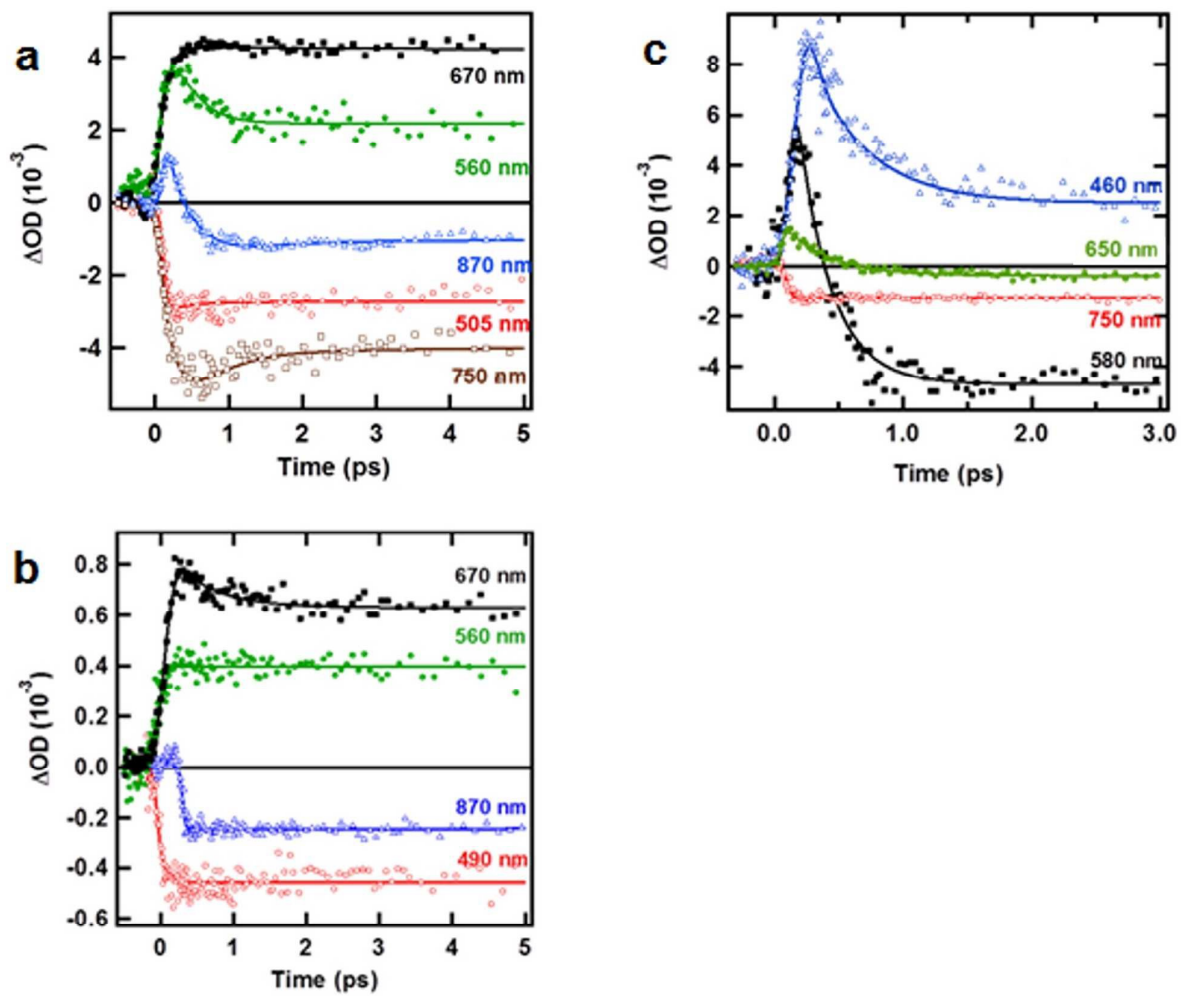


Figure 3

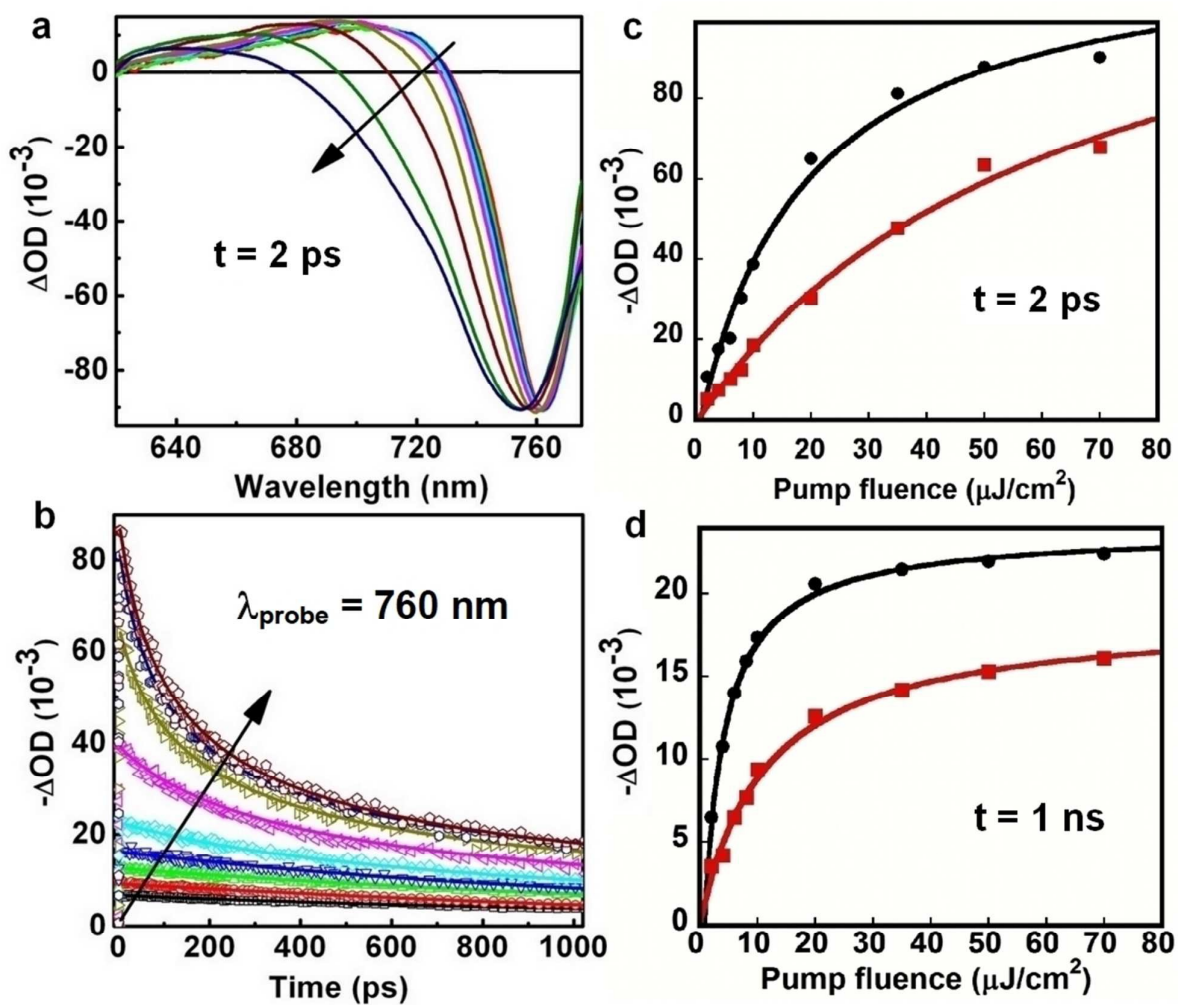


Figure 4

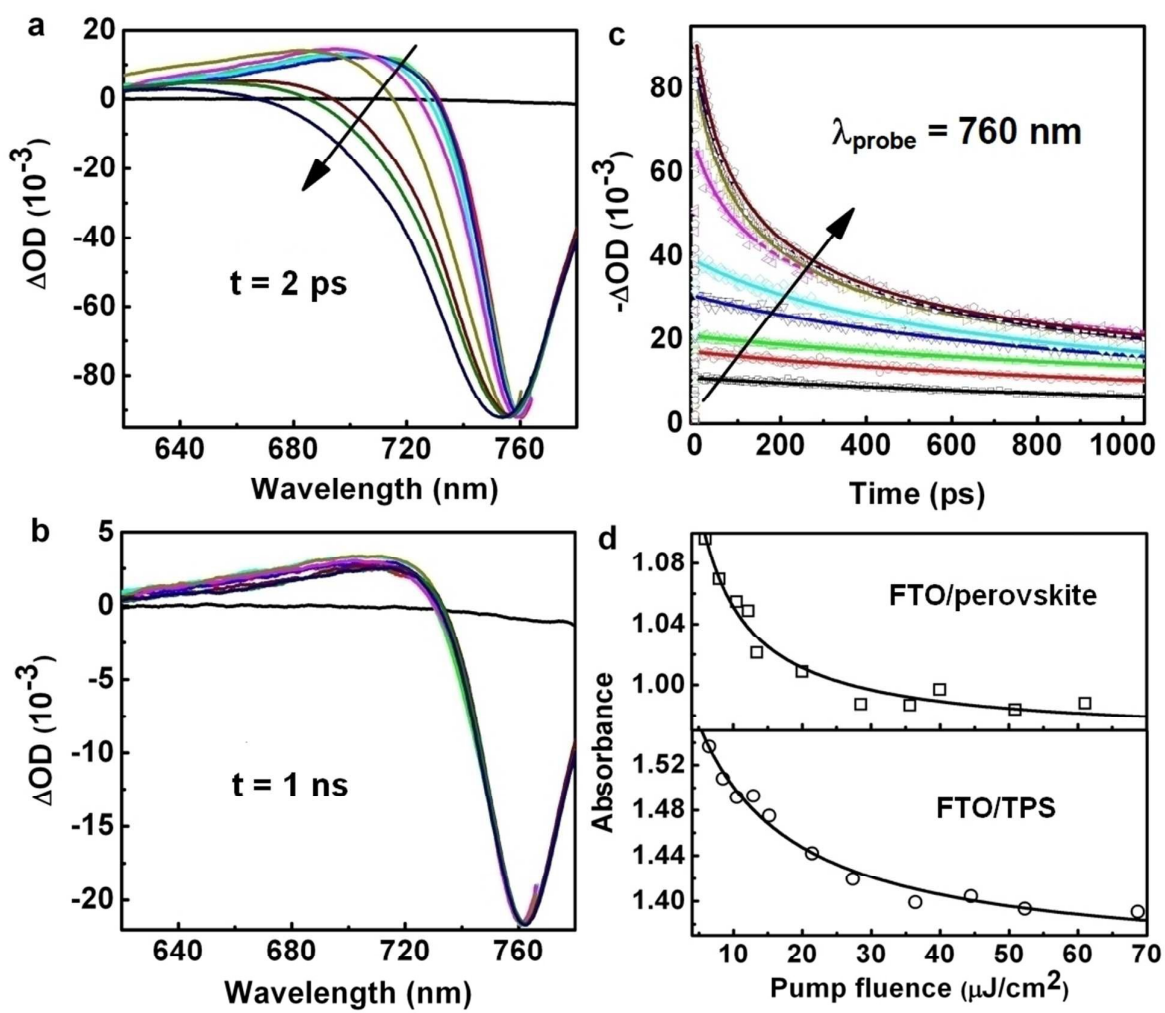


Figure 5

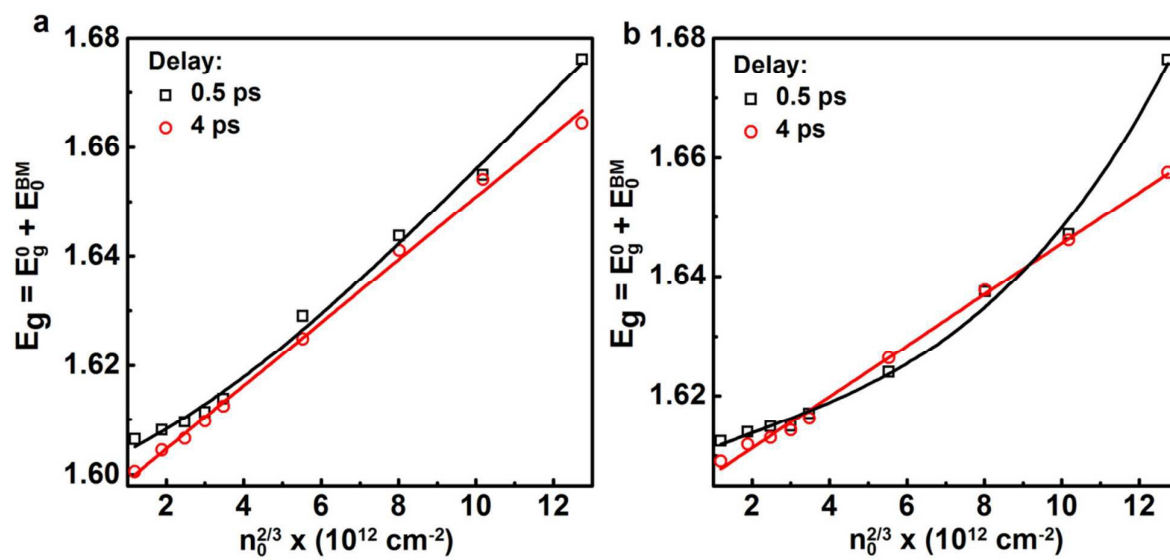


Figure 6

